


## Validation of implosion modeling through direct-drive shock timing experiments at the National Ignition Facility

A. Srinivasan<sup>1</sup>,\* T. R. Boehly<sup>1</sup>, M. C. Marshall<sup>1</sup>, D. N. Polsin<sup>1</sup>, P. B. Radha,<sup>†</sup> M. J. Rosenberg, A. Shvydky, D. Cao, V. N. Goncharov, S. X. Hu<sup>1</sup>, J. Marozas, S. Miller<sup>1</sup>, and S. P. Regan  
*University of Rochester, Laboratory for Laser Energetics, Rochester, New York 14623-1299, USA*

P. M. Celliers, D. E. Fratanduono, and M. Hohenberger  
*Lawrence Livermore National Laboratory, Livermore, California 94550, USA*

 (Received 23 December 2023; accepted 4 April 2024; published 24 April 2024)

Precise modeling of shocks in inertial confinement fusion implosions is critical for obtaining the desired compression in experiments. Shock velocities and postshock conditions are determined by laser-energy deposition, heat conduction, and equations of state. This paper describes experiments at the National Ignition Facility (NIF) [E. M. Campbell and W. J. Hogan, *Plasma Phys. Control. Fusion* **41**, B39 (1999)] where multiple shocks are launched into a cone-in-shell target made of polystyrene, using laser-pulse shapes with two or three pickets and varying on-target intensities. Shocks are diagnosed using the velocity interferometric system for any reflector (VISAR) diagnostic [P. M. Celliers *et al.*, *Rev. Sci. Instrum.* **75**, 4916 (2004)]. Simulated and inferred shock velocities agree well for the range of intensities studied in this work. These directly-driven shock-timing experiments on the NIF provide a good measure of early-time laser-energy coupling. The validated models add to the credibility of direct-drive-ignition designs at the megajoule scale.

DOI: [10.1103/PhysRevE.109.045209](https://doi.org/10.1103/PhysRevE.109.045209)

### I. INTRODUCTION

A spherical capsule is driven by a laser in inertial confinement fusion with the goal of producing more energy from fusion neutrons than the on-target laser energy [1]. In such implosions, ablation of the outer target material drives the shell inward like a rocket. The kinetic energy of the imploding shell is converted into the internal energy of the hot spot, resulting in high ( $\sim$ keV) temperatures in the hot core and, consequently, in fusion reactions. Target performance is quantified using the generalized Lawson criterion parameter as

$$\chi = (\rho R)^{0.61} (0.12Y_{16}/M_{\text{stag}}^{\text{DT}})^{0.34}, \quad (1)$$

where the areal density  $\rho R = \int_0^R \rho(r) dr$ ,  $\rho(r)$  is the mass density as a function of radius  $r$ , and  $R$  is the outer radius of the compressed shell;  $\rho R$  is therefore a measure of the compression of the shell;  $Y_{16}$  is the number of neutrons from the deuterium tritium (DT) fusion reactions in the hot spot in units of  $10^{16}$ , and  $M_{\text{stag}}^{\text{DT}}$  is the unablated DT fuel mass that stagnates [2]. A value of  $\chi = 1$  corresponds to ignition.

Implosions hydrodynamically scaled from ignition designs are performed on the OMEGA laser [3] at energies  $\sim$ 30 kJ. These experiments have reached a value of  $\chi = 0.86$  [4], when hydrodynamically scaled up to an energy of 2.15 MJ. A series of focused experiments studying different physics including shock timing has contributed significantly to target design [5]. These implosions cannot ignite however, since the

OMEGA laser is only capable of  $\sim$ 30 kJ of energy, which is insufficient for ignition. Similar experiments are needed at the megajoule (MJ) scale to validate target designs. As is shown in this paper and in previous work on OMEGA [6–8], shock velocities are extremely sensitive to the heat conducted by nonlocal electrons from the laser deposition region to the ablation surface. The nonlocality of electrons becomes significant when their mean-free path  $\lambda_e \sim T_e/|\nabla T_e|$ , where  $T_e$  is the electron temperature and  $\nabla T_e$  is the gradient of the electron temperature in the coronal plasma. The temperatures and scale lengths determining these gradients differ significantly across energy scales [9], making it important to validate the nonlocal model at the MJ scale. In this paper, results from experiments and simulations are presented for shock timing experiments from the MJ-scale National Ignition Facility (NIF) [10].

As Eq. (1) indicates, both yield and compression are necessary for ignition. The strength and timing of the initial shocks launched by the laser drive “condition” the shell and fuel to obtain maximum compression. Accurate shock timing is critical for setting the compression of the shell in implosion experiments. The design of shock timing in implosions is identified using separate targeted experiments that use interferometric methods. In these experiments, a probe laser incident onto the converging shocks is used to interferometrically measure the time-resolved shock velocities. These measurements track multiple shock waves as they traverse the target, providing both their strength and arrival times.

Results from direct-drive shock timing experiments on the NIF and comparisons with simulation are presented in this work. The NIF is configured for the cylindrical geometry of indirect drive, with cones of beams arranged around the upper and lower poles, with no beams near

\*Also at California Institute of Technology, Pasadena, CA 91125, USA.

<sup>†</sup>rbah@lle.rochester.edu

the equator. This design is to irradiate vertical, cylindrical hohlraums with laser entrance holes at the top and bottom. For direct-drive experiments, the polar-centric beams are redirected toward the equator so as to irradiate the entire surface of a spherical target. Both the energy and temporal pulse shape of all beams are adjusted to produce near-uniform irradiation over the entire sphere. This method is called polar direct drive (PDD) [9,11] and has been modeled significantly. To account for the asymmetry introduced by the NIF PDD geometry, the two-dimensional (2D) axisymmetric arbitrary Lagrangian Eulerian code DRACO [12] is used to design, simulate, and interpret the experiments presented in this paper.

Previous direct-drive shock timing experiments [6–8] have been conducted on the OMEGA laser, where the default geometry of the OMEGA laser is 60 beams arranged spherically symmetrically around the target, also called spherical direct drive (SDD). Most shock timing work on OMEGA, supporting the ongoing cryogenic implosion experiments [4], is based on this geometry and therefore uses the spherically symmetric code LILAC [13] for design instead of the 2D code DRACO. Limited shock timing studies in PDD geometry have also been conducted [14] on OMEGA by deliberately omitting beams from the SDD geometry to mimic the NIF PDD geometry. The models in DRACO compared very well with these experiments. As motivated earlier, however, dedicated PDD shock timing experiments on the NIF are needed to validate the models at the MJ scale, which are presented in this paper.

This work explores four different pulse shapes, each of which includes a series of short laser pulses called “pickets.” The four pulse shapes differ in the number of pickets, their timing, and their peak intensity. These peak intensities are characteristic of designs typically used in direct-drive cryogenic implosions. The powers of the different cones are adjusted to systematically change the symmetry of the shocks transiting through the shell. Beam displacements (or pointings) are kept constant for all of these experiments. Two different axes of the velocity interferometric system for any reflector (VISAR) diagnostic [15–17] are used to simultaneously measure shock velocities at the pole and equator in PDD geometry. Simulations and the physics of the phase of the implosion characterized by shock transit in the shell are described in Sec. II. In Sec. III, the experimental configurations are described. Comparisons with the experimentally measured shock velocities are described in Sec. IV. Conclusions are presented in Sec. V.

## II. SHOCK DYNAMICS

Typical direct-drive implosion designs use a series of multiple pickets followed by a “main pulse” [Fig. 1(a)] [5]. Ignition-relevant targets imploded by such a pulse include a cryogenic deuterium tritium layer encased in a polymeric layer such as polystyrene (abbreviated as CH to represent a polymer of equal number of atoms of carbon and hydrogen) [Fig. 1(b)]. Figure 1(c) is a plot of the density (black) in a cross section of the target (showing the various layers) at 6 ns. Each picket launches a shock [Fig. 1(c)], producing a discontinuity of the pressure (right) at  $\sim 6$  ns. The discontinuity in density even when the pressure is continuous in Fig. 1(c) corresponds to the CH-DT interface and is not a shock [corresponding to

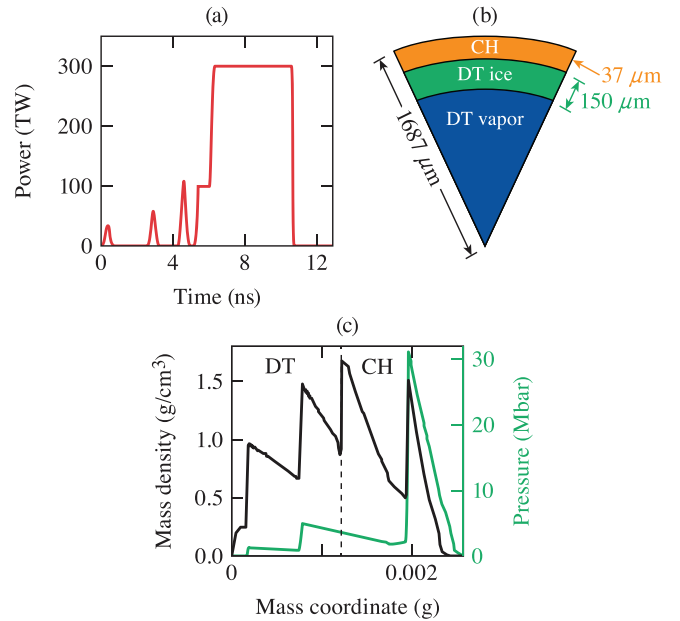


FIG. 1. (a) A laser-pulse shape characterized by three pickets and a main pulse. (b) Target configuration driven by the triple-picket design includes an outer ablator made of a polymeric material comprising carbon and hydrogen, an inner cryogenic deuterium-tritium layer, and residual vapor. (c) At  $\sim 6$  ns, several shocks traverse the ablator and ice. Each shock, characterized by a density jump (left axis) and pressure (right axis), is launched by the three pickets and the main pulse. The vertical dashed line shows the location of the interface between CH and DT.

the dashed line in Fig. 1(c)]. For an efficient and well-tuned design, it is important that these multiple shocks coalesce within the outer part of the vapor region encased by the cryogenic layer. If this coalescence is mistimed, it will adversely increase the adiabat (defined as the ratio of the pressure to the Fermi-degenerate pressure) on the inner surface of the shell, thereby reducing compression. The design shown in Fig. 1, including the individual picket power and width or, alternatively, the picket energy, and the time spacing between them, is determined using the spherically symmetric radiation hydrodynamic code, LILAC [13].

Both LILAC and DRACO include models describing the deposition of the laser energy, heat conduction from the deposited region to the ablation surface, and equations of state (EOS) of the materials involved. Collisional absorption is the primary mechanism for laser-energy deposition during pickets (and at other times when laser-plasma instabilities do not influence the energy deposition). Nonlocal electron heat conduction that accounts for the energetic tail of the electron distribution is also modeled [18,19]. Different equations-of-state (EOS) including SESAME [20] and the first-principles equation of state (FPEOS) [21] are also included in these codes.

Experiments in SDD geometry using a wide range of picket energies and timing were previously performed [8,19] on the OMEGA laser and show reasonable agreement for a large class of laser parameters. A limited set of shock timing measurements in PDD geometry have been performed

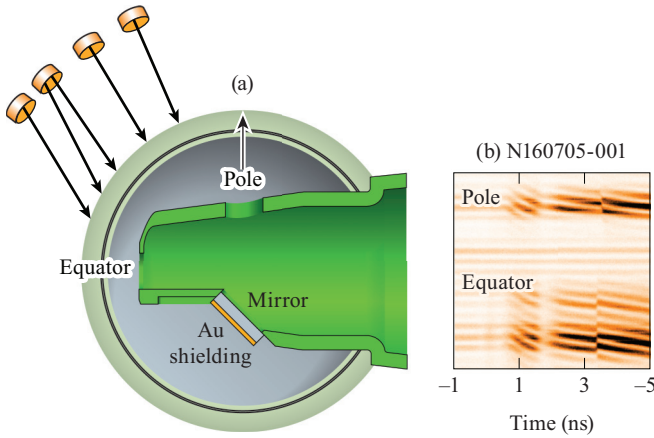


FIG. 2. (a) Schematic showing the experimental setup. The laser is incident on the target, excluding the region occupied by the cone (shown in green). The VISAR laser is incident from the right, probing the regions marked by the equator and the pole. Arrows indicate the beam repointing needed to improve on-target laser symmetry. Each on-target beam is characterized by a beam size that is approximately the size of the target. (b) Time-resolved raw VISAR data for shot N160705-001. The two-axis VISAR provides shock timing and velocity measurements at the pole (top) and equator (bottom) by spatially separating the two signals using a mirror.

on OMEGA in room-temperature CH shells [14]. In these experiments, shocks were viewed only from one angle, i.e., the equator, limited due to the target size on OMEGA. For the larger NIF targets, shocks are viewed simultaneously from two directions, i.e., the equator and the pole on each shot.

### III. EXPERIMENTAL DESIGN AND CONFIGURATION

This paper discusses the results and analysis of four NIF shock timing experiments, using room-temperature 150- $\mu\text{m}$ -thick CH shells and irradiated with multiple pickets, each  $\sim 500$  ps in width. The target is a CH shell with an embedded cone, whose purpose is to prevent the laser irradiation from interfering with the VISAR shock-velocity diagnostic. A schematic of the experimental setup is shown in Fig. 2. The NIF beams are chosen so that they irradiate the sections of the target viewed by the VISAR laser. The arrows represent a schematic of the PDD beam pointing. The introduction of a mirror, shown in Fig. 2, splits the VISAR laser so as to simultaneously view the pole and the equator. It is important to note that the VISAR detects only the leading (front-most) shock wave. Subsequent shocks are detected when they overtake that front shock. This coalescence is noted as a jump in shock velocity and provides a register of “shock timing.” In an ideal implosion, these series of shock overtakes occur in a tight sequence at a prescribed location within the target.

In these experiments, the interferometer detects Doppler shifts of the 660-nm probe beam reflected off the hot, reflective leading shock front in the 150- $\mu\text{m}$ -thick CH shell. An example of the raw VISAR data is shown in Fig. 2(b) for shot N160705-001. The first picket at 0 ns launches the first shock that initially “blanks” the VISAR until the fringe motion is recovered after  $\sim 500$  ps. This leading decaying shock is tracked until 3.4 ns, when the second shock catches up to the first

TABLE I. Displacements of quads in each of the upper-hemispheric cones in NIF geometry.

Original cone angle ( $^\circ$ )	Repointed angle ( $^\circ$ )
23.5	23.5
30	35
44.5	46, 69
50	83

shock. When the second picket laser pulse is on (1.75 ns), it causes the VISAR to temporarily lose contrast. The sensitivities or velocities per fringe ( $\text{VPF}_0$ ) of the two VISAR channels are 13.64  $\mu\text{m}/\text{ns}/\text{fringe}$  and 34.05  $\mu\text{m}/\text{ns}/\text{fringe}$ . The sensitivity is corrected for the refractive index of unshocked CH,  $n$ , and is given by  $\text{VPF} = \text{VPF}_0 \times (n - 1)$ , where  $n = 1.59$ . The fringe phase uncertainty is taken to  $\pm 5\%$  of the more sensitive leg corresponding to 0.68  $\mu\text{m}/\text{ns}$ . The uncertainty in VISAR timing is calculated to be  $\pm 80$  ps. VISAR measurement of shock velocities is a well-established technique. More details of this diagnostic can be found in Refs. [6,15–17]. The NIF beam geometry is arranged in “cones,” where each cone consists of “quads” or groups of four beams incident at a specific latitude on the target. In PDD geometry, beams are displaced in polar and azimuthal angles to improve spherical symmetry. The beam displacements used in this work are summarized in Table I and shown schematically in Fig. 2(a). The first column lists the original angles of incidence on target for each cone, whereas the second column lists the repointed locations of the cones on target. The quad at 44.5 $^\circ$  is split with two beams displaced to different polar angles to improve on-target symmetry. The beams are equally spaced in azimuthal angles. Beams in the northern and southern hemispheres are displaced symmetrically (the cones in the southern hemisphere are not shown in the table). Note that the inner cones predominately irradiate the pole, whereas the outer cones irradiate the equator. Herein, the relative energies between the inner and outer cones will be used dictate the balance of drive at the pole and equator.

In addition to beam displacements, the beam energies for each of the cones are varied. Four different variations of picket energies have been studied in these experiments. As-shot pulse shapes averaged over all the beams within each cone are shown in Fig. 3. The variations are also summarized in Table II for easier reference. For the first case (shot N151025-003), all cones are kept at the nominally identical pulse shape [variations in Fig. 3(a)] due to the on-shot pulse shape delivered by the laser, which differs somewhat from the design. The first picket energy for the second shot [shot N151026-002 in Fig. 3(b)] is deliberately reduced for the inner cones by 20%. This value of 20% is chosen such that the reduced polar shock velocity can be observably diagnosed. Again, variations within the pulse shape for each cone are due to different on-shot pulse shapes delivered by the NIF laser. The third shot [N160705-001 in Fig. 3(c)] retains the same picket energies for all the beams, but increases the peak energy to  $1 \times 10^{14}$  W/cm $^2$  for the two pickets. Finally, the fourth shot (N161031-003) uses triple pickets with varying intensity.

TABLE II. Picket variation for the four shots.

Shot no.	No. pickets	Pulse shapes	Picket intensity [ $\times 10^{13}$ (W/cm <sup>2</sup> )]
N151025-003	2	All cones have the same picket energy and timing	5
N151026-002	2	Inner cones have lower energy pickets by 20%, outer cones have the same energy as N151025-003	Inner cones: 4; outer cones: 5
N160705-001	2	All cones have the same picket energy and timing	10
N161031-003	3	All cones have the same picket energy and timing	$5 \leq I \leq 10$

#### IV. SIMULATIONS AND COMPARISON TO EXPERIMENTAL RESULTS

Post-shot simulations for the NIF experiments are performed with DRACO using as-shot laser-pulse power history. Simulations indicate that the models that can potentially influence the results include the inverse bremsstrahlung laser-deposition model, thermal conduction, and the EOS of the plastic. Laser deposition is modeled with a 3D ray trace [22] with inverse bremsstrahlung as the deposition mechanism. Cross-beam energy transfer [23], a laser-plasma effect where ion-acoustic waves mediate the energy transfer from the incident rays and the outgoing (refracted) rays therefore reducing the deposited laser energy, is not significant for this stage of the implosion since the picket intensities are low and the coronal density scale lengths are still relatively small.

There are two models for heat conduction in DRACO. First is a flux-limited heat-conduction model where the heat flux is defined as  $q = \min(q_{SH}, f q_{FS})$ , where the Spitzer-Harm

heat flux  $q_{SH} = -\kappa \nabla T_e$ ,  $T_e$  is the electron temperature, and  $\kappa$  is the heat-conduction coefficient. The free-streaming heat flux is defined as  $f q_{FS} = f n T_e V_T$ , with  $n$  being the electron density,  $V_T$  the electron thermal velocity, and the chosen value of the flux limiter [24]  $f = 0.06$  in this work. The second is a diffusion-based nonlocal heat-conduction model. Details of this model can be found in [18].

The sensitivity to the two heat-conduction models for low-intensity-pickets two-picket designs [Fig. 3(a)] is shown in Fig. 4. In the two simulations shown in this figure, only the heat-conduction model is varied; all other physics are kept the same. The coronal temperatures are shown in Figs. 4(a) and 4(b) at 500 ps (at the time of the peak power for the first picket). The displacement of the beams and the increased beam overlap near the equator result in higher temperatures than at the pole for both models (left: flux-limited heat conduction; right: nonlocal heat-conduction model). The relatively low peak coronal temperatures of  $\sim 1$  keV, however, result in relatively small nonlocal effects, in contrast to the high-intensity pickets described later. This is evident in Figs. 4(c) and 4(d) where the shock velocities are relatively insensitive to the heat-conduction model. Recall that shock velocity (strength) is driven by ablation, which in turn depends

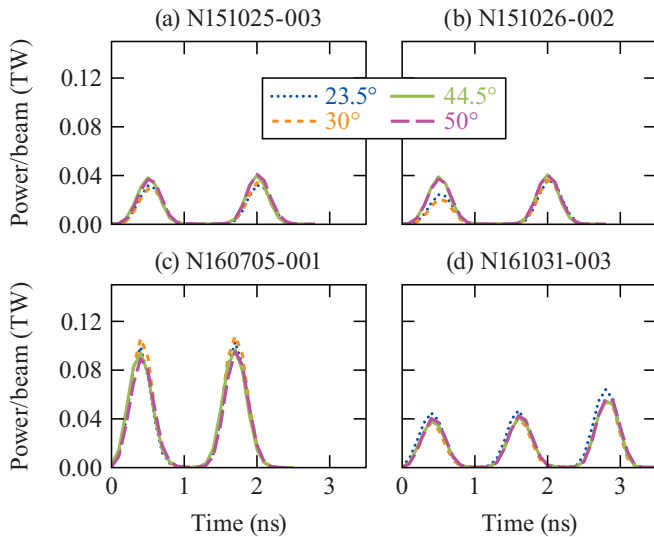


FIG. 3. Experimental pulse shapes from the four NIF shots considered in this work showing single-beam power from each cone vs time. (a) Shot N151025-003: low-intensity ( $5 \times 10^{13}$  W/cm<sup>2</sup>) double pickets, where the different cones have nominally the same picket energies. (b) Shot N151026-002: low-intensity double pickets, where the inner cones have lower picket intensities compared to the outer cones for the first picket. (c) Shot N160705-001: high-intensity double pickets ( $1 \times 10^{14}$  W/cm<sup>2</sup>), with nominally the same energies for all the cones. (d) Shot N161031-003: triple-picket pulse shapes, where the intensities are varied between  $5 \times 10^{13}$  W/cm<sup>2</sup> and  $1 \times 10^{14}$  W/cm<sup>2</sup>.

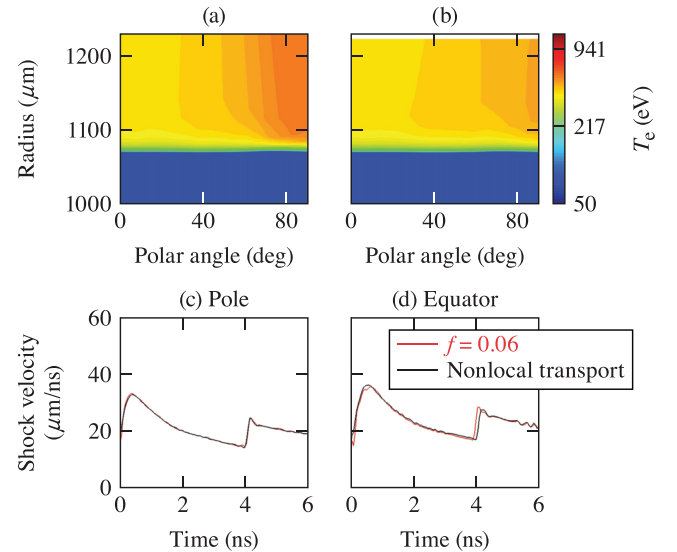


FIG. 4. Sensitivity of shock velocities for low-intensity pickets. (a) Electron-temperature contours in the corona for flux-limited heat conduction. (b) Electron temperature in the corona for the nonlocal heat conduction. (c) Calculated shock velocity with the two heat-conduction models at the pole. (d) Calculated shock velocity with the two heat-conduction models at the equator.

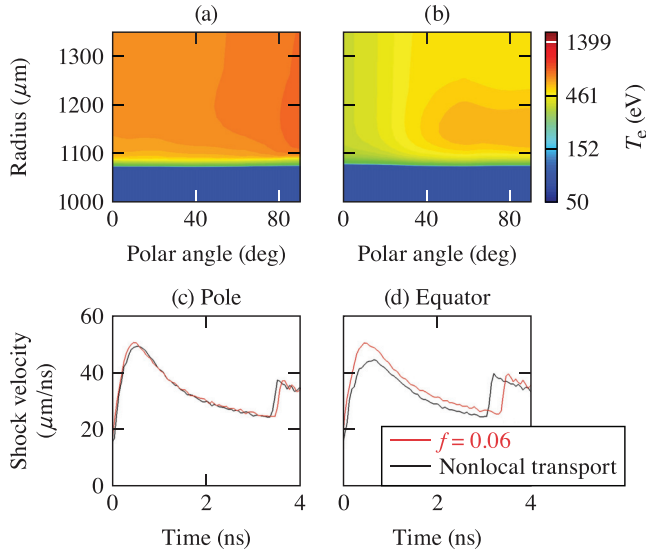


FIG. 5. Sensitivity of shock velocities for high-intensity pickets. (a) Electron-temperature contours in the corona for flux-limited heat conduction. (b) Electron temperature in the corona for nonlocal heat conduction. (c) Calculated shock velocity with the two heat-conduction models at the pole. (d) Calculated shock velocity with the two heat-conduction models at the equator.

on heat conduction from the coronal region. Hence, shock velocity can be a sensitive measure of the laser-absorption and heat-conduction processes.

The sensitivity of the heat-conduction model for the higher-intensity double pickets [Fig. 3(c)] is shown in Fig. 5. Simulations also indicate a transverse temperature gradient for the higher-intensity pickets for both models. In this case, however, the first shock velocity is significantly lower for the nonlocal model compared to the flux-limited heat-conduction model at the equator and the catch-up of the second shock is earlier because of this lower first shock velocity predicted with the nonlocal model. This difference is significant, based on the errors quoted earlier, and can be discerned using VISAR.

Next, the sensitivity to EOS is studied by invoking two different EOS models in the code: FPEOS [21] and SESAME [20]. The comparison of shock timing for SESAME and FPEOS for the low-intensity pickets is shown in Fig. 6.

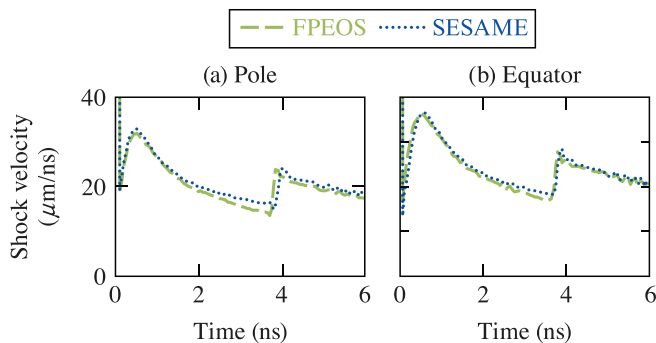


FIG. 6. Shock velocity for the low-intensity pickets for different equations of state; green is the FPEOS model, whereas blue is the SESAME model. (a) The pole and (b) the equator.

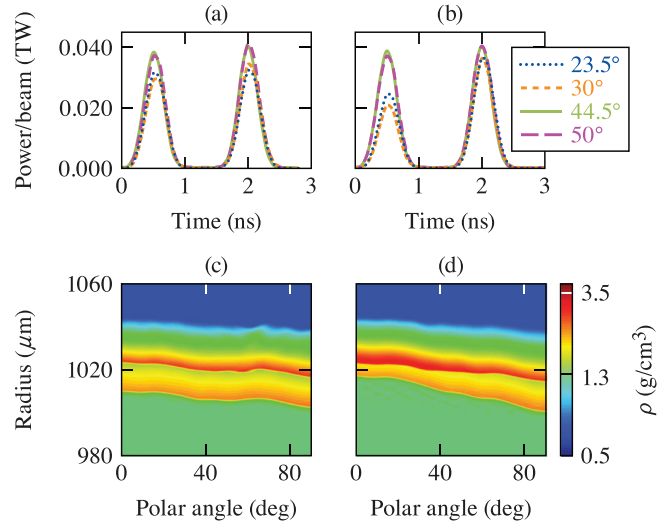


FIG. 7. Contour plots showing mass density vs the radius (y axis) and polar angle (x axis) from simulations for shots corresponding to the lower-intensity double-picket pulse shapes at 3 ns [Figs. 3(a) and 3(b)]. (a) The pole corresponds to  $0^\circ$ , the equator is at  $90^\circ$ . When the first-picket energies for the pole are decreased, the first shock slows advancing the catch-up time at the pole, while the equatorial shock positions remain unchanged.

SESAME results in an observably higher first shock velocity at the pole, whereas the equator is less affected. Again, this difference between the two models at the poles should be observably different. A similar difference is simulated for the higher-intensity two-picket design.

Contour plots of mass density are shown in Fig. 7 for the two shots with varying first-picket energies in the inner cones. The distinct changes in the color indicate the location of the two shocks from each of the pickets. A lower first-picket energy results in a slower shock and therefore a shock that is less converged (at a larger radius) at the pole [Fig. 7(b)] compared to the shock position for the higher picket energy [Fig. 7(a)]. The picket energies are unchanged at the equator and the shock positions there are relatively unchanged.

Experimentally measured shock velocities for the two picket cases (when only the inner cones have similar energies to the outer cones, and the case when the inner-cone picket energy is reduced by 20%) are shown in Fig. 8. The trends are consistent with predictions of the design. The equatorial shock velocities in Fig. 8(a) are relatively unchanged since the pickets energies that dominantly irradiate the equator are nominally identical for the two cases. The polar shock velocities [Fig. 8(b)] are decreased when the inner-cone (polar) picket energies are reduced by 20%.

Next, simulations are compared with experiments. All simulations subsequently presented use DRACO, including inverse bremsstrahlung laser deposition, nonlocal heat conduction, and the FPEOS. Remarkably good agreement is obtained for the shock velocity and shock catch-up time for the low-intensity equal-energy double pickets, shown in Fig. 9. As mentioned earlier, note that the experimental uncertainty in shock velocity is of the order of the thickness of the line. The SESAME EOS (which drives a faster shock), shown in Fig. 6,

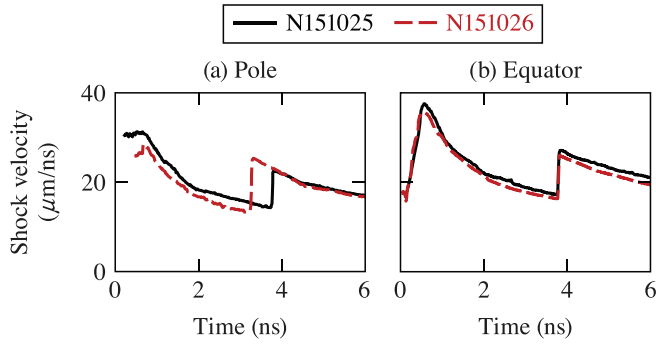


FIG. 8. Comparison of experimentally inferred shock velocities when only the inner-cone power is changed. (a) Polar shock velocities and (b) equatorial shock velocities. Shot N151025 has 20% higher inner-cone energy than N151026. The uncertainty in shock velocity is calculated to be  $0.68 \mu\text{m/ns}$  (within the thickness of the lines) and time is  $\pm 80 \text{ ps}$ .

is clearly precluded as an appropriate model when compared to experimental shock velocities, particularly at the pole. An appropriate heat-conduction model that works for a range of designs cannot be identified based on this intensity alone since the shock velocities are insensitive to the heat-conduction model (Fig. 4).

The agreement at the pole and equator persists even for the pulse shape when the first-picket energy in the inner cones is reduced by 20% (Fig. 10). For this shot, the shock catch-up at the pole is advanced by nearly 500 ps relative to the shot with the same cone picket energies. This 500-ps advance is also captured very well with simulations. Again, the choice of an appropriate heat-conduction model can be made only with higher-intensity pickets, as shown previously.

Simulated shock velocities and experimentally inferred velocities for the higher-intensity pickets are compared in Fig. 11 for shot N160705-001. The simulated shock is marginally faster for the first shock at the pole compared to experiment. The shock catch-up is modeled well, whereas the combined shock velocity is marginally higher in the simulation. This difference is smaller than the difference between the two heat-conduction models shown in Fig. 5, suggesting that the nonlocal model is the more appropriate choice for modeling heat conduction for these experiments. The

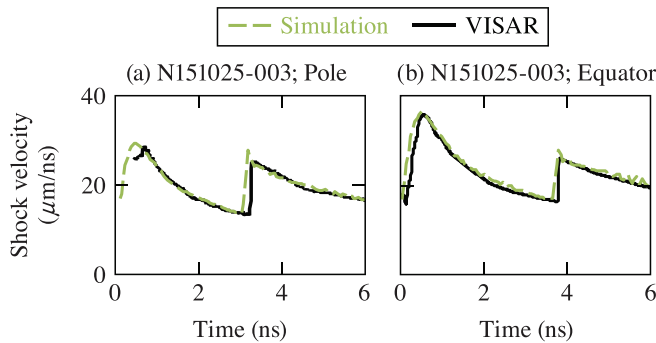


FIG. 9. Shock velocity for the low-intensity pickets for shot N151025. Simulation in green and experiment in black for (a) the pole and (b) the equator.

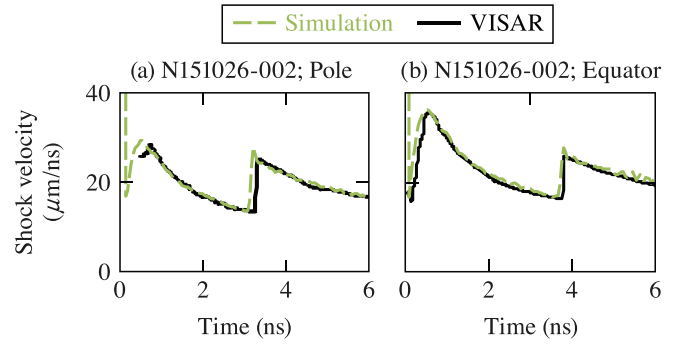


FIG. 10. Simulation (green) compared to experimental velocity (black) for N151026-002. (a) Polar shock velocity. (b) Equatorial shock velocity. The first discontinuity at  $\sim 3.5 \text{ ns}$  corresponds to the shock from the second picket catching up with the shock from the first picket.

simulated shock velocity and catch-up compares very well with the experimental shock velocities at the equator, indicating again that nonlocal thermal conduction more accurately models the experiment.

The reason for the discrepancy at the pole at this higher intensity is unclear. As Fig. 5 indicates, the polar shock velocities are insensitive to the heat-conduction model. Since this difference is based on only a single shot, it may be possible that there are unknowns in the experiment resulting in this difference. Repeating this shot might shed light on this difference.

The variation of the picket-beam energies between the various quads could also provide a potential source of difference in shock timing. The effect of these multidimensional effects, such as the power imbalance between the quads, was modeled with 10 random realizations of picket energy with a standard deviation of 10% rms, typical of the NIF picket energy variations in these experiments. These simulations did not significantly influence the shock velocities. Therefore, the power imbalance between the different cones does not likely explain the difference observed for the polar velocities between simulation and experiment. Additional experiments

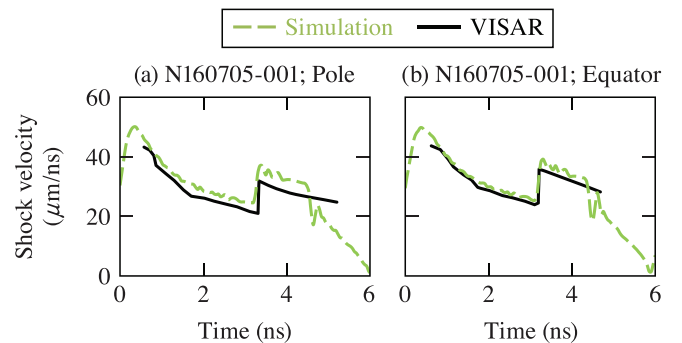


FIG. 11. Shock velocity for the high-intensity pickets for shot N160705 (with picket intensity of  $1 \times 10^{14} \text{ W/cm}^2$ ). Simulation in green and experiment in black for (a) the pole and (b) the equator. The first discontinuity at  $\sim 3.5 \text{ ns}$  corresponds to the shock from the second picket catching up with the shock from the first picket.

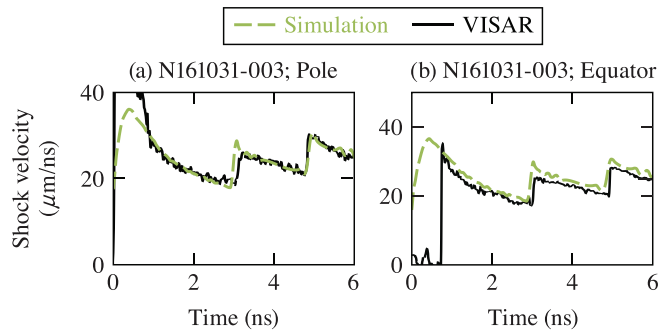


FIG. 12. Shock velocity for the low-intensity pickets for shot N161031. Simulation in green and experiment in black. (a) Shock velocity at the pole. (b) Shock velocity at the equator. The first discontinuity at  $\sim 3.5$  ns corresponds to the shock from the second picket catching up with the shock from the first picket, and the second discontinuity at  $\sim 4.5$  ns corresponds to the shock from the third picket catching up with the earlier shock.

to repeat these pulse-shape parameters are needed to pin down this difference.

Finally, shock velocities from the simulation and experiment for the triple-picket shot are shown in Fig. 12. Excellent agreement is obtained for this case, also indicating that the combination of inverse bremsstrahlung laser deposition, non-local heat conduction, and the FPEOS models shock timing for a range of on-target picket intensities. These results with multiple shocks also indicate that post-shock conditions are also modeled well for these experiments.

## V. SUMMARY AND CONCLUSIONS

Accurate shock timing is important to achieve predictive compression in laser-driven inertial confinement fusion implosions. Previously, experiments on the OMEGA laser have been used to develop models and identify target designs for implosion experiments on OMEGA (kJ scale). The identification of ignition-relevant MJ-scale direct-drive target

designs requires the validation of physics models, including those that are used to time shocks in implosion designs. A set of focused direct-drive shock timing experiments at the National Ignition Facility in polar-direct-drive geometry is reported here. Pulse shapes with either two or three pickets with differing on-target intensities are used to drive shocks in a plastic ablator. VISAR measurements of shock velocity and timing are used to gauge the efficacy of various models. Simulations were performed using the radiation hydrodynamic code DRACO that includes a 3D-ray trace, models of heat conduction including a flux-limited diffusive model and a nonlocal diffusive model, and EOS including SESAME and FPEOS. The DRACO simulations including FPEOS and nonlocal heat conduction are in good agreement with the experimental data, validating these models at ignition scale for direct-drive implosions.

## ACKNOWLEDGMENTS

This material is based upon work supported by the U.S. Department of Energy (National Nuclear Security Administration), University of Rochester “National Inertial Confinement Program” under Award No. DE-NA0004144 and under the auspices of the U.S. Department of Energy by Lawrence Livermore National Laboratory under Contract No. DE-AC52-07NA27344. This report was prepared as an account of work sponsored by an agency of the U.S. Government. Neither the U.S. Government nor any agency thereof, nor any of their employees, makes any warranty, express or implied, or assumes any legal liability or responsibility for the accuracy, completeness, or usefulness of any information, apparatus, product, or process disclosed, or represents that its use would not infringe privately owned rights. Reference herein to any specific commercial product, process, or service by trade name, trademark, manufacturer, or otherwise does not necessarily constitute or imply its endorsement, recommendation, or favoring by the U.S. Government or any agency thereof. The views and opinions of the authors expressed herein do not necessarily state or reflect those of the U.S. Government or any agency thereof.

- [1] J. Nuckolls, L. Wood, A. Thiessen, and G. Zimmerman, Laser compression of matter to super-high densities: Thermonuclear (CTR) applications, *Nature (London)* **239**, 139 (1972).
- [2] P. Y. Chang, R. Betti, B. K. Spears, K. S. Anderson, J. Edwards, M. Fatenejad, J. D. Lindl, R. L. McCrory, R. Nora, and D. Shvarts, Generalized measurable ignition criterion for inertial confinement fusion, *Phys. Rev. Lett.* **104**, 135002 (2010).
- [3] R. Boehly, D. L. Brown, R. S. Craxton, R. L. Keck, J. P. Knauer, J. H. Kelly, T. J. Kessler, S. A. Kumpan, S. J. Loucks, and S. A. Letzring *et al.*, Initial performance results of the OMEGA laser system, *Opt. Commun.* **133**, 495 (1997).
- [4] V. Gopalaswamy, C. A. Williams, R. Betti, D. Patel, J. P. Knauer, A. Lees, D. Cao, E. M. Campbell, P. Farnakis, R. Ejaz *et al.*, Demonstration of a hydrodynamically equivalent burning plasma in direct-drive inertial confinement fusion, *Nat. Phys.* (2024).
- [5] R. S. Craxton, K. S. Anderson, T. R. Boehly, V. N. Goncharov, D. R. Harding, J. P. Knauer, R. L. McCrory, P. W. McKenty, D. D. Meyerhofer *et al.*, Direct-drive inertial confinement fusion: A review, *Phys. Plasmas* **22**, 110501 (2015).
- [6] T. R. Boehly, V. N. Goncharov, W. Seka, S. X. Hu, J. A. Marozas, D. D. Meyerhofer, P. M. Celliers, D. G. Hicks, M. A. Barrios, D. Fratanduono, and G. W. Collins, Multiple spherically converging shock waves in liquid deuterium, *Phys. Plasmas* **18**, 092706 (2011).
- [7] V. N. Goncharov, T. C. Sangster, T. R. Boehly, S. X. Hu, I. V. Igumenshchev, F. J. Marshall, R. L. McCrory, D. D. Meyerhofer, P. B. Radha, W. Seka *et al.*, Demonstration of the highest deuterium-tritium areal density using multiple-picket cryogenic designs on OMEGA, *Phys. Rev. Lett.* **104**, 165001 (2010).
- [8] D. Cao, T. R. Boehly, M. C. Gregor, D. N. Polsin, A. K. Davis, P. B. Radha, S. P. Regan, and V. N. Goncharov, Theoretical

- quantification of shock-timing sensitivities for direct-drive inertial confinement fusion implosions on OMEGA, *Phys. Plasma* **25**, 052705 (2018).
- [9] P. B. Radha, M. Hohenberger, D. H. Edgell, J. A. Marozas, F. J. Marshall, D. T. Michel, M. J. Rosenberg, W. Seka, A. Shvydky, T. R. Boehly *et al.*, Direct drive: Simulations and results from the national ignition facility, *Phys. Plasmas* **23**, 056305 (2016).
- [10] E. M. Campbell, and W. J. Hogan, The National Ignition Facility-applications for inertial fusion energy and high-energy-density science, *Plasma Phys. Control. Fusion* **41** B39 (1999).
- [11] S. Skupsky, J. A. Marozas, R. S. Craxton, R. Betti, T. J. B. Collins, J. A. Delettrez, V. N. Goncharov, P. W. McKenty, P. B. Radha, T. R. Boehly *et al.*, Polar direct drive on the National Ignition Facility, *Phys. Plasmas* **11**, 2763 (2004).
- [12] P. B. Radha, V. N. Goncharov, T. J. B. Collins, J. A. Delettrez, Y. Elbaz, V. Yu. Glebov, R. L. Keck, D. E. Keller, J. P. Knauer, J. A. Marozas *et al.*, Two-dimensional simulations of plastic-shell, direct-drive implosions on OMEGA, *Phys. Plasmas* **12**, 032702 (2005).
- [13] J. Delettrez, R. Epstein, M. C. Richardson, P. A. Jaanimagi, and B. L. Henke, Effect of laser illumination nonuniformity on the analysis of time-resolved x-ray measurements in UV spherical transport experiments, *Phys. Rev. A* **36**, 3926 (1987).
- [14] P. B. Radha, F. J. Marshall, T. R. Boehly, T. J. B. Collins, R. S. Craxton, D. Edgell, R. Epstein, J. Frenje, V. N. Goncharov, and J. A. Marozas, Polar drive on OMEGA, *EPJ Web Conf.* **59**, 02013 (2013).
- [15] P. M. Celliers, D. K. Bradley, G. W. Collins, D. G. Hicks, T. R. Boehly, and W. J. Armstrong, Line-imaging velocimeter for shock diagnostics at the OMEGA laser facility, *Rev. Sci. Instrum.* **75**, 4916 (2004).
- [16] D. H. Munro, P. M. Celliers, G. W. Collins, D. M. Gold, L. B. Da Silva, S. W. Haan, R. C. Cauble, B. A. Hammel, and W. W. Hsing, Shock timing techniques for the National Ignition Facility, *Phys. Plasmas* **8**, 2245 (2001).
- [17] H. F. Robey, T. R. Boehly, P. M. Celliers, J. H. Eggert, D. Hicks, R. F. Smith, R. Collins, M. W. Bowers, K. G. Krauter, P. S. Datte *et al.*, Shock timing experiments on the National Ignition Facility: Initial results and comparison with simulation, *Phys. Plasmas* **19**, 042706 (2012).
- [18] D. Cao, G. Moses, and J. Delettrez, Improved nonlocal thermal transport model for two-dimensional radiation hydrodynamic simulations, *Phys. Plasmas* **22**, 082308 (2015).
- [19] V. N. Goncharov, O. V. Gotchev, E. Vianello, T. R. Boehly, J. P. Knauer, P. W. McKenty, P. B. Radha, S. P. Regan, T. C. Sangster, and S. Skupsky, Early stage of implosion in inertial confinement fusion: Shock timing and perturbation evolution, *Phys. Plasmas* **13**, 012702 (2006).
- [20] S. P. Lyon and J. D. Johnson, Los Alamos National Laboratory, Los Alamos, CA, Report No. LA-UR-92-3407 (1992), See, also, J. D. Johnson and S. P. Lyon, National Technical Information Service Document No. DE85014241 (1985). Copies may be obtained from the National Technical Information Service, Springfield, VA 22161, USA (1992).
- [21] S. X. Hu, L. A. Collins, V. N. Goncharov, J. D. Kress, R. L. McCrory, and S. Skupsky, First-principles equation of state of polystyrene and its effect on inertial confinement fusion implosions, *Phys. Rev. E* **92**, 043104 (2015).
- [22] J. A. Marozas, M. Hohenberger, M. J. Rosenberg, D. Turnbull, T. J. B. Collins, P. B. Radha, P. W. McKenty, J. D. Zuegel, F. J. Marshall, S. P. Regan *et al.*, Wavelength-detuning cross-beam energy transfer mitigation scheme for direct drive: Modeling and evidence from National Ignition Facility implosions, *Phys. Plasmas* **25**, 056314 (2018).
- [23] I. V. Igumenshchev, W. Seka, D. H. Edgell, D. T. Michel, D. H. Froula, V. N. Goncharov, R. S. Craxton, L. Divol, R. Epstein, R. Follett *et al.*, Crossed-beam energy transfer in direct-drive implosions, *Phys. Plasmas* **19**, 056314 (2012).
- [24] R. C. Malone, R. L. McCrory, and R. L. Morse, Indications of strongly flux-limited electron thermal conduction in laser-target experiments, *Phys. Rev. Lett.* **34**, 721 (1975).